Journal of Alloys and Compounds 968 (2023) 171903

Contents lists available at ScienceDirect

Journal of Alloys and Compounds

journal homepage: www.elsevier.com/locate/jalcom

# Single crystal growth and characterization of topological semimetal ZrSnTe

Sudip Acharya [a], Krishna Pandey [a], Rabindra Basnet [b], Gokul Acharya [b], Md Rafique Un Nabi [b], Jian Wang [c], Jin Hu [a,b,*]

[a] Materials Science and Engineering Program, Institute for Nanoscience and Engineering, University of Arkansas, Fayetteville, AR 72701, USA
[b] Department of Physics, University of Arkansas, Fayetteville, AR 72701, USA
[c] Department of Chemistry and Biochemistry, Wichita State University, Wichita, KS 67260, USA

ARTICLE INFO

*Keywords:*
ZrSnTe
Topological materials
Single crystal growth

ABSTRACT

High quality single crystals are critical for experimental materials science research. ZrSnTe represents such an example. This material belongs to the ZrSiS-type topological material family, which is so far the only one in this material family possessing Fermi surface formed by Dirac bands generated by a Sn-square net. Experimental study on ZrSnTe is limited due to the difficulty in single crystal growth. In this work, we report the single crystal growth for ZrSnTe using a solid-state reaction method with Sn as a flux. The roles of various growth parameters such as the molar ratio of starting materials, growth temperature and cooling rate in obtaining sizeable single crystals were investigated. The quality of the obtained single crystals was checked by elemental, structural and electronic characterizations. Our study on the growth method for ZrSnTe would enable the future study on this less explored topological semimetal.

## 1. Introduction

Topological insulators (TIs) have attracted extensive interests from the scientific community [1]. The study of topological materials has not only been limited to 2D and 3D TIs, but has been extended to the topological semimetals (TSMs) such as Dirac semimetals [2,3] and Weyl semimetals [4,5]. TSMs host relativistic fermions with linear energy-momentum dispersions that are analogous to Dirac and Weyl fermions in high energy physics [2,6]. Such Dirac and Weyl states are protected by certain symmetries, and display numerous exotic properties such as large magnetoresistance [7], high mobility [7], chiral anomaly [8–11], and surface Fermi arcs [12–16]. Unlike Dirac and Weyl semimetals showing linearly dispersed band crossings at discrete points in the momentum space, another category of TSMs known as the nodal-line semimetals (NLSMs) exhibit linear band crossings along a one-dimensional loops or lines.

A family of NLSMs, represented by the chemical formula *WHM* (*W* = Zr/Hf/rare earth, *H* = Si/Ge/Sn/Sb, *M* = O/S/Se/Te) [17–28] have attracted intensive attention in recent years. *WHM* materials mainly possess a similar tetragonal structure with the space group *P4/nmm*, except some exhibiting orthorhombic distortions. Those materials crystallize in layered structures, with the square or nearly square lattice layers of *H* atoms sandwiched by *W-M* layers. Some *WHM* compounds, such as ZrSiSe and ZrSiTe, show rather weak inter-layer coupling, thus enabling mechanical exfoliation to obtain atomically thin flakes [22,29]. Two types of Dirac states have been discovered in *WHM*s, including the gapless Dirac point states protected by non-symmorphic symmetry, and the slightly gapped Dirac nodal-line states generated by the glide mirror symmetry [19,21]. Interesting properties such as the surface floating bands [29,30], enhanced electronic correlations [31–33], and pressure-induced topological phase transitions [34,35] have been discovered in *WHM* compounds. Furthermore, magnetism can also be induced into this system by magnetic rare earth elements. The isostructural or structurally similar *Ln*SbTe (*Ln* = lanthanides) compounds represents magnetic version of *WHM* materials [25,26,36–47] which also exhibit topological electronic states [25,26,36,46,47]. The composition non-stoichiometry and 4*f*-magnetism greatly enrich these *Ln*SbTe materials with various quantum phenomena such as the interplay between topological states with charge density waves [38,40,41] and enhanced electronic correlations [36,43,46].

Among various *WHM* topological materials, ZrSnTe is so far the only one that is characterized by the Sn square lattice in its crystal structure. Band structure calculations have revealed that the Fermi surface for ZrSnTe is formed only by Dirac bands in a scenario similar to ZrSiS [19,

* Corresponding author at: Materials Science and Engineering Program, Institute for Nanoscience and Engineering, University of Arkansas, Fayetteville, AR 72701, USA.
*E-mail address:* jinhu@uark.edu (J. Hu).

https://doi.org/10.1016/j.jallcom.2023.171903
Received 7 May 2023; Received in revised form 28 July 2023; Accepted 25 August 2023
Available online 28 August 2023
0925-8388/

48], which is not widely seen in topological materials and make this material a good platform to study the behavior of pure Dirac electrons without any interference from conventional non-relativistic electrons. Despite those unique properties and the fact that ZrSnTe is among the first few predicted *WHM*-type topological materials [19,48], the experimental studies on this material are rather rare [18,49,50]. This could be attributed to the difficulty in obtaining high quality large single crystals for ZrSnTe. Distinct from other *WHM* materials whose single crystals are synthesized by using chemical vapor transport (CVT) methods, single crystals for ZrSnTe are reported to be grown by flux methods using Te [18] or Sn [49,50] flux. However, the much less studies on ZrSnTe compared to other *WHM*s imply the crystal growth could be the major challenge.

In this work, we focus on investigating the single crystal growth for ZrSnTe, with a goal of obtaining reproducible method to grow sizable single crystals for ZrSnTe and clarify the important parameters that affect the crystal growth. Our work demonstrates Sn is an effective flux for ZrSnTe growth, and the temperature ramping rate plays a vital role for the crystal growth. This discovery paves a way for future studies on fairly under-explored ZrSnTe topological material.

## 2. Methods and results

During the investigation of the single crystals for ZrSnTe, in order to identify the optimize the growth method and eliminate any extrinsic factors, we have been carefully to use the same source material, mixing procedure, etc. Single crystals of ZrSiS family are typically synthesized by a CVT method using halides as a transport agent [51]. We have also adopted a similar method to grow single crystals for ZrSnTe but have never been able to obtain ZrSnTe crystals. So, we switched to the flux method where individual materials melt at high temperatures, and during cooling nucleation takes places which leads to crystallization of the desired phase. In order to minimize the impurities brought in by the flux, here we focus on a self-flux method which utilizes the constitute elements of the target compound as the flux. For ZrSnTe, both Sn and Te are potential flux due to their low melting points (Sn: ~232 °C, Te: ~450 °C). In fact, both Te [18] and Sn [49,50] fluxes have been reported. In this work, we explored both fluxes and found that Te-flux never resulted in ZrSnTe crystals for any amount of flux. For example, using an atomic ratio of Zr:Sn:Te = 1:1:10 or 1:1:20 only led to $ZrTe_2$. In contrast, our initial trial using Sn flux successfully produced some ZrSnTe single crystals. Therefore, we focus on optimizing Sn-flux growth for ZrSnTe.

The flux method for single crystal growth has been well-established. In this work, we adopted the standard method [51,52] for the metal Sn flux growth for ZrSnTe. During the metal flux growth for single crystals, the source materials are mixed with the flux and loaded in an alumina crucible, which is covered by a catch crucible on top of it to collect the excess flux in the subsequent centrifuge process. A spacer with hole(s) is placed in between the crucibles to catch the crystals during centrifuge. The crucibles are sealed in an evacuated quartz tube as shown in Fig. 1 (a). At an appropriate reaction temperature, the flux melts and the source materials react and dissolve in the flux. Up on cooling, single crystals start to precipitate from the melts, which can be separated from the molten flux by decanting and centrifuge. During this process, the quartz tube is inverted and placed in a centrifuge. Single crystals are caught by the spacer and the excess flux is captured by the catch crucible, as illustrated in Fig. 1(a).

For flux growth for single crystals, several parameters play important roles, such as the reaction temperature $T_r$, the centrifuge temperature $T_c$, cooling rate, and the amount of flux. $T_r$ must be sufficiently high to melt and dissolve source materials in flux but should not be too high to avoid the softening of the quartz tube. $T_c$ must be above the melting point of the flux to separate the obtained crystals from the flux but should not be too high to allow sufficient precipitate and nucleation of the target crystals. The amount of flux should be adequate to efficiently dissolve

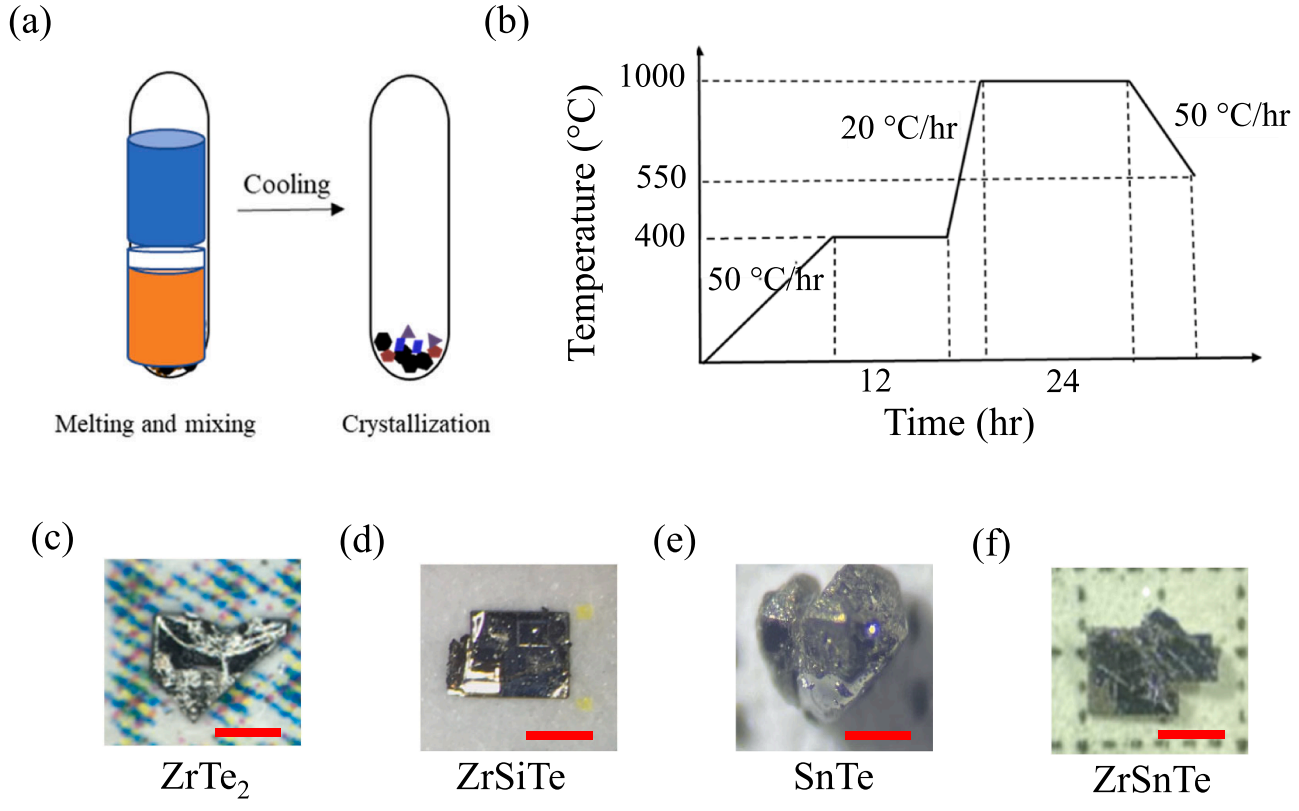


**Fig. 1.** (a) Schematic diagram of single crystal growth using a flux method. (b) Heating profile for the growth of ZrSnTe crystals. Optical microscope images of as-obtained single crystals of (c) $ZrTe_2$, (d) ZrSiTe, (e) SnTe and (f) ZrSnTe. Scale bar: 1 mm.

source materials or precursors at a reasonable temperature, though it is limited by the size of a crucible. It is worth noting that all growth parameters are not independent from each other. For example, $T_r$ might be lowered when flux amount is increased, which could be helpful to avoid the formation of some unwanted phases at certain temperature regions. For the ternary compound ZrSnTe, the growth is even more challenging, due to the complication of the unwanted binary byproducts which can be easily formed.

To grow ZrSnTe using Sn-flux, we chose the highest growth temperature $T_r = 1000$ °C and the centrifuge temperature $T_c = 550$ °C. We found that slight deviation of $T_r$ by 50 °C or so did not affect the growth. For the centrifuge temperature, we adopted a temperature much higher than the melting point of Sn flux (~ 232 °C), because the quartz tube cools quickly during the transfer from the furnace to the centrifuge. In addition, higher $T_c$ might also be helpful to reduce the formation of the unwanted SnTe phase (melting point ~790 °C).

With the determined $T_r$ and $T_c$, we have performed multiple growths with various flux amount and cooling rates. In Table 1 we summarized the 24 representative growths with varying the ratio of source material Zr:Sn:Te = 1:4:1, 1:5:1, 1:6:1 and 1:10:1, and the cooling rate 10, 20, 30, 40, 50, and 60 °C/hour. The phase of the obtained crystals is characterized by Energy dispersive x-ray spectroscopy (EDS) and *x*-ray diffraction (XRD) analyses. Generally, lower cooling rate not only favors better crystallinity, but also increased domain size due to reduced nucleation centers. However, we found that a cooling rate of 40 °C/hour and below cannot yield ZrSnTe. Instead, secondary phases such as $ZrTe_2$ and SnTe were obtained for various flux amounts, as summarized in Table 1, and shown in Fig. 1(c-e). In addition, we also obtained ZrSiTe crystals in some growths, for which the Si might come from the quartz wools which were used to secure the position of the crucibles inside the quartz tube. Their compositions were determined by EDS as shown in Fig. 2(a). Among those secondary phases, the formation of ZrSiTe might be attributed to the partial reaction of the source material and quartz wool used for flux growth. To eliminate certain phases such as SnTe with a higher melting point of ~790 °C, we tried to centrifuge at higher temperature when SnTe is not expected to precipitate. However, such an attempt did not yield ZrSnTe crystals either.

In contrast, single crystals for ZrSnTe were successfully obtained with increasing cooling rate to 50 °C/hour. The stoichiometric composition of the obtained ZrSnTe single crystals were confirmed by using EDS, which yielded a composition of $Zr_{1.007}Sn_{0.998}Te_{1.005}$. Although the formation of ZrSiTe with very low cooling rate raises concerns of Si incorporation, we did not observe clearly signature of Si in ZrSnTe obtained with fast cooling, as shown in the EDS spectra in Fig. 2(a). One possible reason is that the lower cooling rates may favor the reaction of source material and the quartz wool which consumes Zr and Te sources, which hinders the formation of ZrSnTe. It is worth noting that cooling too fast is not favorable for ZrSnTe growth as well. In fact, we found that increasing the cooling rate by another 10 °C/hour did not yield visible crystals, which is understandable because it needs a certain period for nucleation and condensation to form crystals of reasonable sizes, and a 10 °C increase means increasing the rate by 20%.

Compared to the cooling rate, the amount of flux, i.e., the ratio of source materials and the Sn flux, seems not to significantly affect the formation of the desired ZrSnTe phase, as summarized in Table 1. At a lower cooling rate (such as 5 °C/hour), varying the Zr:Sn:Te ratio form 1:4:1–1:10:1 only leads to various secondary phase. At a cooling rate of 50 °C/hour when we obtained the ZrSnTe crystals, low flux amount leads to few crystals while too much flux (such as Zr:Sn:Te = 1:10:1) causes significant Sn flux residual after centrifuge. We found that a ratio of Zr:Sn:Te = 1:6:1 is the most appropriate to grow ZrSnTe single crystals. An image of such a crystal is shown in Fig. 1(f).

These results suggest that the crystal growth mechanism of ZrSnTe is complicated. The two important parameters, reactant/flux ratio and cooling rate are coupled together. Since slow cooling always resulted in impurity phases (see Table 1). Hence, the target ZrSnTe phase might be a metastable phase, which favors fast cooling. The best synthetic condition would be loading Zr/Sn/Te= 1:6:1 with a cooling rate of 50 °C/hr with cooling down from 1000 °C to 550 °C. Based on Sn-Te phase diagram [53], the thermodynamically stable SnTe forms from 670 °C to 550 °C when the molar ratio of Sn/Te= 6:1. SnTe was also observed during our experiments (Table 1). Based on Sn-Zr phase diagram [53], the thermodynamic stable $ZrSn_2$ forms from 1000 °C to 550 °C when the molar ratio of Sn/Zr= 6:1. Hence, during the cooling down process, all these thermodynamically stable compounds such as SnTe and $ZrSn_2$ competed with the target ZrSnTe phase, which might explain why slow cooling does not work in our study. A faster cooling rate (60 °C/hr), however, may result in too fast spontaneous nucleation, which would lead to numerous small crystals [54] of various phases. To better clarify the mechanism, additional study such as crystal growth aided by in situ powder x-ray diffraction is necessary [55].

To verify the crystal structure, we performed single crystals XRD. The refined crystal structure confirmed the desired tetragonal layered structure of our ZrSnTe, as shown in Fig. 2(b). The structure parameters are shown in Table 2 and in the supplementary materials. Furthermore, we have performed Raman spectroscopy study (Fig. 2(c)), from which three major vibrational modes centered around 119, 138, and 193.2 $cm^{-1}$ are observed. The observed Raman spectrum for ZrSnTe is very different from other *WHM* compounds such as ZrSiS [56], ZrSiSe [57], ZrSiTe [58], suggesting the variation from Si- to Sn-square net may significantly affect the lattice vibration modes in *WHM* compounds.

To characterize the quality of the obtained ZrSnTe crystals, we have measured their electronic transport properties. The in-plane resistivity measurements yield a metallic transport behavior with a residual resistivity of 4.5 μΩ cm [Fig. 3(a), Left Panel]. The resistivity value is a few times lower than the previous report [49]. Such difference can be attributed to many reasons, such as the error in estimation of the same size as well as the variation of sample quality. From the measurements on multiple pieces of crystals, we found that crystals grown with large amounts of flux usually exhibit a superconducting transition around 3.9 K. One example (sample S1) is shown in Fig. 3(a). Such superconducting transition should be attributed to the residual Sn flux present on the surface of ZrSnTe crystals, because sample grown with less amount of Sn flux and with Sn flux carefully removed do not show superconductivity down to 2 K (e.g., sample S2 in Fig. 3a). The magneto-transport revealed a normalized magnetoresistance MR = $[\rho(B)-\rho(B=0\ T)]/\rho(B=0\ T)$ of ~ 18% at $T = 2$ K and $B = 9$ T, which is suppressed with increasing temperature, reaching 2% at 300 K at 9 T. Such MR values are much smaller than that for ZrSiS [22,59,60] and ZrSiSe [20,61] but comparable to ZrSiTe [20].

The Hall effect measurements reveal a linear field dependence for Hall resistivity $\rho_{xy}$, as shown in Fig. 4(a). Such linear Hall resistivity persist down to $T = 2$ K, which is in sharp contrast to ZrSiS [20,61], ZrSiSe [20,22,59], and ZrSiTe [22] that display non-linear field dependence at low temperatures. The positive slope of $\rho_{xy}(B)$ indicates that the transport is dominated by holes, from which the hole densities

**Table 1**
Summary of various Sn-flux growth with varying flux amount and cooling rate. The grow temperature $T_r$ and the centrifuge temperature $T_c$ are fixed to 1000 °C and 550 °C, respectively.

| | Zr:Sn:Te | | | |
|---|---|---|---|---|
| Cooling rate | 1:4:1 | 1:5:1 | 1:6:1 | 1:10:1 |
| 5 °C/hr | ZrSiTe, $ZrTe_2$ | ZrSiTe | ZrSiTe, SnTe | SnTe |
| 10 °C/hr | no crystal | no crystal | no crystal | no crystal |
| 20 °C/hr | no crystal | no crystal | no crystal | no crystal |
| 40 °C/hr | no crystal | no crystal | no crystal | no crystal |
| 50 °C/hr | few small crystals | few small crystals | large crystals | large crystals with Sn on surface |
| 60 °C/hr | no crystal | no crystal | no crystal | no crystal |

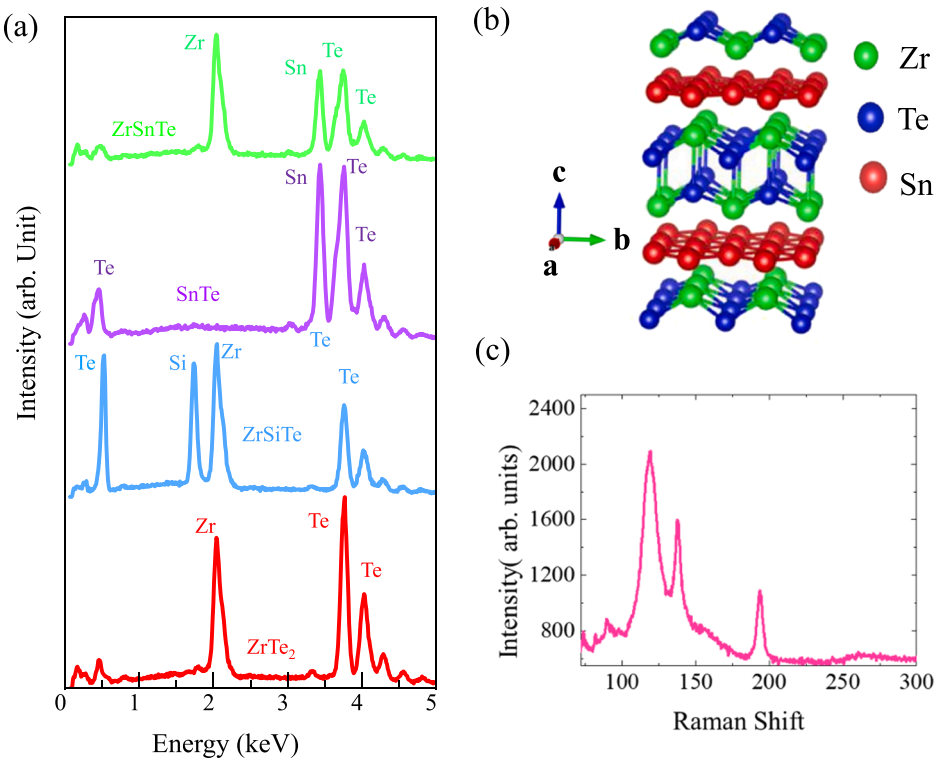


**Fig. 2.** (a) EDS spectra of ZrSnTe single crystal.(b) Crystal structure of a ZrSnTe single crystal (c) Raman spectra of ZrSnTe single crystal.

**Table 2**
Crystallographic data for tetragonal ZrSnTe obtained from single crystal XRD refinement.

| Element | Wyckoff | *x* | *y* | *z* | $U_{eq}$ (Å$^2$) | Occupancy |
|---|---|---|---|---|---|---|
| Zr | 2c | 0.2500 | 0.2500 | 0.7349 | 0.0133(17) | 1 |
| Sn | 2a | -0.2500 | 0.2500 | 1.0000 | 0.0133(16) | 1 |
| Te | 2c | 0.2500 | 0.2500 | 0.3807 | 0.0117(17) | 1 |

Space group: *P4/nmm*. Lattice parameters: $a = 4.0598(3)$ Å, $b = 4.0598(3)$ Å, c= *8*.7049(9) Å. Data collection temperature: 296(2)K. Radiation wavelength: 1.54178 Å. $R_1 = 0.0538$, $WR_2 = 0.1209$.

at various temperatures can be extracted. As shown in Fig. 4(b), the carrier density is in the order of $10^{21}$ cm$^{-3}$, which is an order of magnitude greater than ZrSiS, ZrSiSe, and ZrSiTe [22] and consistent with the nodal-line band structure for ZrSnTe. From magnetotransport, the carrier mobility at 2 K is found to be 165 cm$^2$/Vs [Fig. 4(b)], which is lower than ZrSi(S,Se,Te). Therefore, it is not surprising that the Shubnikov–de Haas effect is not observed up to 9 T in our magneto-transport study. This is also consistent with the previous discovery of de Haas-van Alphen quantum oscillation above 10 T in magnetic torque measurements [49].

## 3. Conclusion

In conclusion, we investigated the single crystal growth for ZnSnTe. Unlike other related materials that are generally grown by using a chemical vapor transport method, ZrSnTe single crystals were successfully obtained by a flux method with Sn as the flux. We also found that rapid cooling is critical to minimize the secondary phases and yield the desired ZrSnTe phase. Our study on crystal growth for ZrSnTe would pave a way for the future investigation on this less-explored topological material which is the only one that is characterized by the Sn square lattice in *WHM* family.

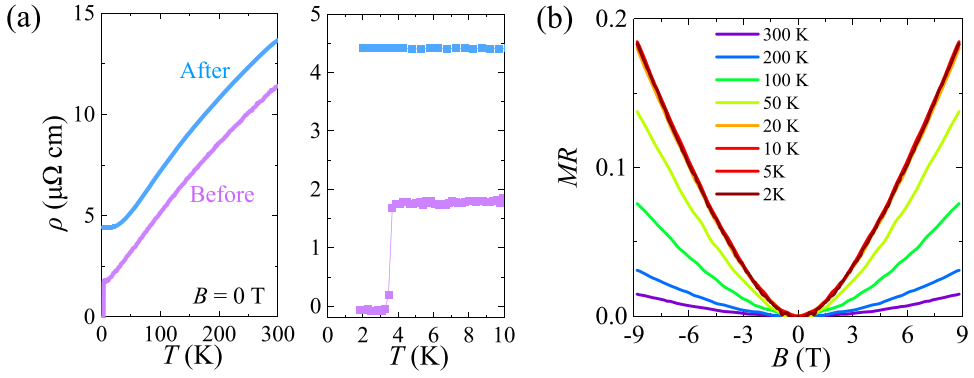


**Fig. 3.** (a) Left panel: Temperature dependence of the electrical resistivity of ZrSnTe single crystals with (S1) and without (S2) Sn surface residual. Right panel: Low temperature resistivity showing superconducting transition at $T \approx 3.9$ K due to Sn flux residual on the surface of the ZrSnTe crystal. (b) Magnetoresistance of ZrSnTe (S2 sample) at different temperatures ranging from 2 K to 300 K.

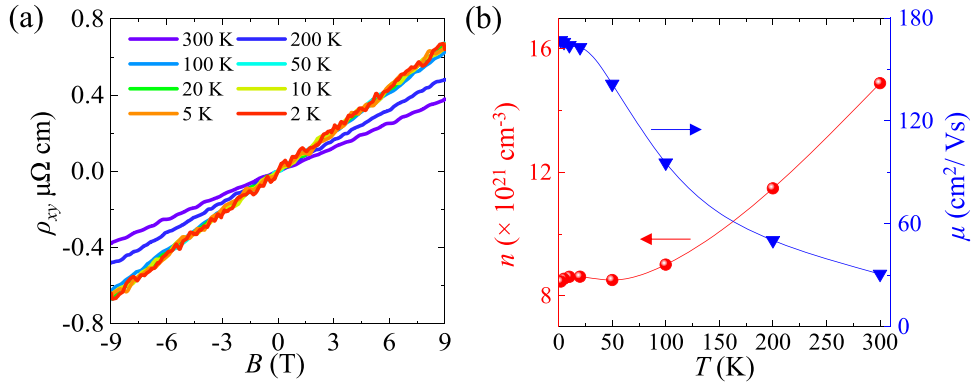


**Fig. 4.** (a) Field dependence of Hall resistivity $\rho_{xy}$ at various temperatures from 2 K to 300 K for ZrSnTe (S2 sample). (b) Evolution of carrier concentration $n$ and mobility μ from 2 K to 300 K.

## CRediT authorship contribution statement

**Sudip Acharya**: Methodology, Investigation, Formal analysis, Writing – original draft. **Krishna Pandey**: Investigation. **Rabindra Basnet**: Investigation. **Gokul Acharya**: Investigation. **Md Rafique Un Nabi**: Investigation. **Jian Wang**: Investigation, Visualization. **Jin Hu**: Conceptualization, Supervision, Resources, Writing – review & editing.

## Declaration of Competing Interest

The authors declare that they have no known competing financial interests or personal relationships that could have appeared to influence the work reported in this paper.

## Data Availability

Data will be made available on request.

## Acknowledgement

This work was primarily (synthesis, characterization, transport) supported by the U.S. Department of Energy, Office of Science, Basic Energy Sciences program under Grant No. DE-SC0022006. J.W. acknowledges the support from the U.S. National Science Foundation under grand DMR-2328822 for single crystal XRD and structure refinement. We thank Prof. Shui-Qing Yu from the University of Arkansas for informative discussions.

## Appendix A. Supporting information

Supplementary data associated with this article can be found in the online version at doi:10.1016/j.jallcom.2023.171903.

## References

[1] J. Ma, K. Deng, L. Zheng, S. Wu, Z. Liu, S. Zhou, D. Sun, Experimental progress on layered topological semimetals, 2D Mater. 6 (2019), 032001, https://doi.org/10.1088/2053-1583/ab0902.
[2] M.Z. Hasan, C.L. Kane, Colloquium: topological insulators, Rev. Mod. Phys. 82 (2010) 3045–3067, https://doi.org/10.1103/RevModPhys.82.3045.
[3] Z.K. Liu, B. Zhou, Y. Zhang, Z.J. Wang, H.M. Weng, D. Prabhakaran, S.-K. Mo, Z. X. Shen, Z. Fang, X. Dai, Z. Hussain, Y.L. Chen, Discovery of a three-dimensional topological dirac semimetal, Na3Bi, Science 343 (2014) 864–867, https://doi.org/10.1126/science.1245085.
[4] H. Weng, C. Fang, Z. Fang, B.A. Bernevig, X. Dai, Weyl semimetal phase in noncentrosymmetric transition-metal monophosphides, Phys. Rev. X. 5 (2015), 011029, https://doi.org/10.1103/PhysRevX.5.011029.
[5] B.Q. Lv, N. Xu, H.M. Weng, J.Z. Ma, P. Richard, X.C. Huang, L.X. Zhao, G.F. Chen, C.E. Matt, F. Bisti, V.N. Strocov, J. Mesot, Z. Fang, X. Dai, T. Qian, M. Shi, H. Ding, Observation of Weyl nodes in TaAs, Nat. Phys. 11 (2015) 724–727, https://doi.org/10.1038/nphys3426.
[6] L. Fu, Topological crystalline insulators, Phys. Rev. Lett. 106 (2011), 106802, https://doi.org/10.1103/PhysRevLett.106.106802.
[7] T. Liang, Q. Gibson, M.N. Ali, M. Liu, R.J. Cava, N.P. Ong, Ultrahigh mobility and giant magnetoresistance in the Dirac semimetal Cd3As2, Nat. Mater. 14 (2015) 280–284, https://doi.org/10.1038/nmat4143.
[8] Q. Li, D.E. Kharzeev, C. Zhang, Y. Huang, I. Pletikosić, A.V. Fedorov, R.D. Zhong, J. A. Schneeloch, G.D. Gu, T. Valla, Chiral magnetic effect in ZrTe5, Nat. Phys. 12 (2016) 550–554, https://doi.org/10.1038/nphys3648.
[9] Y.-S. Jho, K.-S. Kim, Interplay between interaction and chiral anomaly: Anisotropy in the electrical resistivity of interacting Weyl metals, Phys. Rev. B. 87 (2013), 205133, https://doi.org/10.1103/PhysRevB.87.205133.
[10] D.T. Son, B.Z. Spivak, Chiral anomaly and classical negative magnetoresistance of Weyl metals, Phys. Rev. B. 88 (2013), 104412, https://doi.org/10.1103/PhysRevB.88.104412.
[11] R. Roy, C. Kallin, Collective modes and electromagnetic response of a chiral superconductor, Phys. Rev. B. 77 (2008), 174513, https://doi.org/10.1103/PhysRevB.77.174513.
[12] S.-Y. Xu, C. Liu, S.K. Kushwaha, R. Sankar, J.W. Krizan, I. Belopolski, M. Neupane, G. Bian, N. Alidoust, T.-R. Chang, H.-T. Jeng, C.-Y. Huang, W.-F. Tsai, H. Lin, P. P. Shibayev, F.-C. Chou, R.J. Cava, M.Z. Hasan, Observation of Fermi arc surface states in a topological metal, Science 347 (2015) 294–298, https://doi.org/10.1126/science.1256742.
[13] S.-Y. Xu, N. Alidoust, I. Belopolski, Z. Yuan, G. Bian, T.-R. Chang, H. Zheng, V. N. Strocov, D.S. Sanchez, G. Chang, C. Zhang, D. Mou, Y. Wu, L. Huang, C.-C. Lee, S.-M. Huang, B. Wang, A. Bansil, H.-T. Jeng, T. Neupert, A. Kaminski, H. Lin, S. Jia, M. Zahid Hasan, Discovery of a Weyl fermion state with Fermi arcs in niobium arsenide, Nat. Phys. 11 (2015) 748–754, https://doi.org/10.1038/nphys3437.
[14] B.Q. Lv, H.M. Weng, B.B. Fu, X.P. Wang, H. Miao, J. Ma, P. Richard, X.C. Huang, L. X. Zhao, G.F. Chen, Z. Fang, X. Dai, T. Qian, H. Ding, Experimental Discovery of Weyl Semimetal TaAs, Phys. Rev. X. 5 (2015), 031013, https://doi.org/10.1103/PhysRevX.5.031013.
[15] S.-M. Huang, S.-Y. Xu, I. Belopolski, C.-C. Lee, G. Chang, B. Wang, N. Alidoust, G. Bian, M. Neupane, C. Zhang, S. Jia, A. Bansil, H. Lin, M.Z. Hasan, A Weyl fermion semimetal with surface Fermi arcs in the transition metal monopnictide TaAs class, Nat. Commun. 6 (2015) 7373, https://doi.org/10.1038/ncomms8373.
[16] X. Wan, A.M. Turner, A. Vishwanath, S.Y. Savrasov, Topological semimetal and Fermi-arc surface states in the electronic structure of pyrochlore iridates, Phys. Rev. B. 83 (2011), 205101, https://doi.org/10.1103/PhysRevB.83.205101.
[17] D. Takane, Z. Wang, S. Souma, K. Nakayama, C.X. Trang, T. Sato, T. Takahashi, Y. Ando, Dirac-node arc in the topological line-node semimetal HfSiS, Phys. Rev. B. 94 (2016), 121108, https://doi.org/10.1103/PhysRevB.94.121108.
[18] R. Lou, J.-Z. Ma, Q.-N. Xu, B.-B. Fu, L.-Y. Kong, Y.-G. Shi, P. Richard, H.-M. Weng, Z. Fang, S.-S. Sun, Q. Wang, H.-C. Lei, T. Qian, H. Ding, S.-C. Wang, Emergence of topological bands on the surface of ZrSnTe crystal, Phys. Rev. B. 93 (2016), 241104, https://doi.org/10.1103/PhysRevB.93.241104.
[19] Q. Xu, Z. Song, S. Nie, H. Weng, Z. Fang, X. Dai, Two-dimensional oxide topological insulator with iron-pnictide superconductor LiFeAs structure, Phys. Rev. B. 92 (2015), 205310, https://doi.org/10.1103/PhysRevB.92.205310.
[20] M.M. Hosen, K. Dimitri, I. Belopolski, P. Maldonado, R. Sankar, N. Dhakal, G. Dhakal, T. Cole, P.M. Oppeneer, D. Kaczorowski, F. Chou, M.Z. Hasan, T. Durakiewicz, M. Neupane, Tunability of the topological nodal-line semimetal phase in $\mathrm{ZrSi}X$-type materials ($X=\mathrm{S}, \mathrm{Se}, \mathrm{Te}$), Phys. Rev. B. 95 (2017), 161101, https://doi.org/10.1103/PhysRevB.95.161101.
[21] L.M. Schoop, M.N. Ali, C. Straßer, A. Topp, A. Varykhalov, D. Marchenko, V. Duppel, S.S.P. Parkin, B.V. Lotsch, C.R. Ast, Dirac cone protected by non-symmorphic symmetry and three-dimensional Dirac line node in ZrSiS, Nat. Commun. 7 (2016) 11696, https://doi.org/10.1038/ncomms11696.
[22] J. Hu, Z. Tang, J. Liu, X. Liu, Y. Zhu, D. Graf, K. Myhro, S. Tran, C.N. Lau, J. Wei, Z. Mao, Evidence of topological nodal-line fermions in ZrSiSe and ZrSiTe, Phys. Rev. Lett. 117 (2016), 016602, https://doi.org/10.1103/PhysRevLett.117.016602.
[23] M. Neupane, I. Belopolski, M.M. Hosen, D.S. Sanchez, R. Sankar, M. Szlawska, S.-Y. Xu, K. Dimitri, N. Dhakal, P. Maldonado, P.M. Oppeneer, D. Kaczorowski,

F. Chou, M.Z. Hasan, T. Durakiewicz, Observation of topological nodal fermion semimetal phase in ZrSiS, Phys. Rev. B. 93 (2016), 201104, https://doi.org/10.1103/PhysRevB.93.201104.
[24] C. Chen, X. Xu, J. Jiang, S.-C. Wu, Y.P. Qi, L.X. Yang, M.X. Wang, Y. Sun, N.B. M. Schröter, H.F. Yang, L.M. Schoop, Y.Y. Lv, J. Zhou, Y.B. Chen, S.H. Yao, M. H. Lu, Y.F. Chen, C. Felser, B.H. Yan, Z.K. Liu, Y.L. Chen, Dirac line nodes and effect of spin-orbit coupling in the nonsymmorphic critical semimetals $M\mathrm{SiS}\phantom{\rule{0.16em}{0ex}}(M=\mathrm{Hf},\phantom{\rule{0.16em}{0ex}}\mathrm{Zr})$, Phys. Rev. B. 95 (2017), 125126 https://doi.org/10.1103/PhysRevB.95.125126.
[25] M.M. Hosen, G. Dhakal, K. Dimitri, P. Maldonado, A. Aperis, F. Kabir, C. Sims, P. Riseborough, P.M. Oppeneer, D. Kaczorowski, T. Durakiewicz, M. Neupane, Discovery of topological nodal-line fermionic phase in a magnetic material GdSbTe, Sci. Rep. 8 (2018) 13283, https://doi.org/10.1038/s41598-018-31296-7.
[26] L.M. Schoop, A. Topp, J. Lippmann, F. Orlandi, L. Müchler, M.G. Vergniory, Y. Sun, A.W. Rost, V. Duppel, M. Krivenkov, S. Sheoran, P. Manuel, A. Varykhalov, B. Yan, R.K. Kremer, C.R. Ast, B.V. Lotsch, Tunable Weyl and Dirac states in the nonsymmorphic compound CeSbTe, Science Advances. 4 (n.d.) eaar2317. https://doi.org/10.1126/sciadv.aar2317.
[27] B.-B. Fu, C.-J. Yi, T.-T. Zhang, M. Caputo, J.-Z. Ma, X. Gao, B.Q. Lv, L.-Y. Kong, Y.-B. Huang, P. Richard, M. Shi, V.N. Strocov, C. Fang, H.-M. Weng, Y.-G. Shi, T. Qian, H. Ding, Dirac nodal surfaces and nodal lines in ZrSiS, Science Advances. 5 (n.d.) eaau6459. https://doi.org/10.1126/sciadv.aau6459.
[28] A. Topp, J.M. Lippmann, A. Varykhalov, V. Duppel, B.V. Lotsch, C.R. Ast, L. M. Schoop, Non-symmorphic band degeneracy at the Fermi level in ZrSiTe, N. J. Phys. 18 (2016), 125014, https://doi.org/10.1088/1367-2630/aa4f65.
[29] X. Liu, C. Yue, S.V. Erohin, Y. Zhu, A. Joshy, J. Liu, A.M. Sanchez, D. Graf, P. B. Sorokin, Z. Mao, J. Hu, J. Wei, Quantum transport of the 2D surface state in a nonsymmorphic semimetal, Nano Lett. 21 (2021) 4887–4893, https://doi.org/10.1021/acs.nanolett.0c04946.
[30] A. Topp, R. Queiroz, A. Grüneis, L. Müchler, A.W. Rost, A. Varykhalov, D. Marchenko, M. Krivenkov, F. Rodolakis, J.L. McChesney, B.V. Lotsch, L. M. Schoop, C.R. Ast, Surface floating 2D bands in layered nonsymmorphic semimetals: ZrSiS and related compounds, Phys. Rev. X. 7 (2017), 041073, https://doi.org/10.1103/PhysRevX.7.041073.
[31] S. Pezzini, M.R. van Delft, L.M. Schoop, B.V. Lotsch, A. Carrington, M.I. Katsnelson, N.E. Hussey, S. Wiedmann, Unconventional mass enhancement around the Dirac nodal loop in ZrSiS, Nat. Phys. 14 (2018) 178–183, https://doi.org/10.1038/nphys4306.
[32] Y. Shao, A.N. Rudenko, J. Hu, Z. Sun, Y. Zhu, S. Moon, A.J. Millis, S. Yuan, A. I. Lichtenstein, D. Smirnov, Z.Q. Mao, M.I. Katsnelson, D.N. Basov, Electronic correlations in nodal-line semimetals, Nat. Phys. 16 (2020) 636–641, https://doi.org/10.1038/s41567-020-0859-z.
[33] G. Gatti, A. Crepaldi, M. Puppin, N. Tancogne-Dejean, L. Xian, U. De Giovannini, S. Roth, S. Polishchuk, Ph Bugnon, A. Magrez, H. Berger, F. Frassetto, L. Poletto, L. Moreschini, S. Moser, A. Bostwick, E. Rotenberg, A. Rubio, M. Chergui, M. Grioni, Light-induced renormalization of the Dirac Quasiparticles in the nodal-line semimetal ZrSiSe, Phys. Rev. Lett. 125 (2020), 076401, https://doi.org/10.1103/PhysRevLett.125.076401.
[34] D. VanGennep, T.A. Paul, C.W. Yerger, S.T. Weir, Y.K. Vohra, J.J. Hamlin, Possible pressure-induced topological quantum phase transition in the nodal line semimetal ZrSiS, Phys. Rev. B. 99 (2019), 085204, https://doi.org/10.1103/PhysRevB.99.085204.
[35] C.C. Gu, J. Hu, X.L. Chen, Z.P. Guo, B.T. Fu, Y.H. Zhou, C. An, Y. Zhou, R.R. Zhang, C.Y. Xi, Q.Y. Gu, C. Park, H.Y. Shu, W.G. Yang, L. Pi, Y.H. Zhang, Y.G. Yao, Z. R. Yang, J.H. Zhou, J. Sun, Z.Q. Mao, M.L. Tian, Experimental evidence of crystal symmetry protection for the topological nodal line semimetal state in ZrSiS, Phys. Rev. B. 100 (2019), 205124, https://doi.org/10.1103/PhysRevB.100.205124.
[36] K. Pandey, D. Mondal, J.W. Villanova, J. Roll, R. Basnet, A. Wegner, G. Acharya, M. R.U. Nabi, B. Ghosh, J. Fujii, J. Wang, B. Da, A. Agarwal, I. Vobornik, A. Politano, S. Barraza-Lopez, J. Hu, Magnetic topological semimetal phase with electronic correlation enhancement in SmSbTe, Adv. Quantum Technol. 4 (2021) 2100063, https://doi.org/10.1002/qute.202100063.
[37] B. Lv, J. Chen, L. Qiao, J. Ma, X. Yang, M. Li, M. Wang, Q. Tao, Z.-A. Xu, Magnetic and transport properties of low-carrier-density Kondo semimetal CeSbTe, J. Phys.: Condens. Matter 31 (2019), 355601, https://doi.org/10.1088/1361-648X/ab2498.
[38] R. Singha, T.H. Salters, S.M.L. Teicher, S. Lei, J.F. Khoury, N.P. Ong, L.M. Schoop, Evolving Devil's staircase magnetization from tunable charge density waves in nonsymmorphic dirac semimetals, Adv. Mater. 33 (2021) 2103476, https://doi.org/10.1002/adma.202103476.
[39] R. Sankar, I.P. Muthuselvam, K.R. Babu, G.S. Murugan, K. Rajagopal, R. Kumar, T.-C. Wu, C.-Y. Wen, W.-L. Lee, G.-Y. Guo, F.-C. Chou, Crystal growth and magnetic properties of topological nodal-line semimetal GdSbTe with antiferromagnetic spin ordering, Inorg. Chem. 58 (2019) 11730–11737, https://doi.org/10.1021/acs.inorgchem.9b01698.
[40] S. Lei, A. Saltzman, L.M. Schoop, Complex magnetic phases enriched by charge density waves in the topological semimetals ${\mathrm{GdSb}}_{x}{\mathrm{Te}}_{2\ensuremath{-}x\ensuremath{-}\ensuremath{\delta}}$, Phys. Rev. B. 103 (2021), 134418 https://doi.org/10.1103/PhysRevB.103.134418.
[41] S. Lei, V. Duppel, J.M. Lippmann, J. Nuss, B.V. Lotsch, L.M. Schoop, Charge density waves and magnetism in topological semimetal candidates GdSbxTe2−x−δ, Adv. Quantum Technol. 2 (2019) 1900045, https://doi.org/10.1002/qute.201900045.
[42] K. Pandey, R. Basnet, J. Wang, B. Da, J. Hu, Evolution of electronic and magnetic properties in the topological semimetal $\mathrm{Sm}{\mathrm{Sb}}_{x}{\mathrm{Te}}_{2\ensuremath{-}x}$, Phys. Rev. B. 105 (2022), 155139 https://doi.org/10.1103/PhysRevB.105.155139.
[43] K. Pandey, R. Basnet, A. Wegner, G. Acharya, M.R.U. Nabi, J. Liu, J. Wang, Y. K. Takahashi, B. Da, J. Hu, Electronic and magnetic properties of the topological semimetal candidate NdSbTe, Phys. Rev. B. 101 (2020), 235161, https://doi.org/10.1103/PhysRevB.101.235161.
[44] R. Sankar, I.P. Muthuselvam, K. Rajagopal, K. Ramesh Babu, G.S. Murugan, K. S. Bayikadi, K. Moovendaran, C. Ting Wu, G.-Y. Guo, Anisotropic magnetic properties of nonsymmorphic semimetallic single crystal NdSbTe, Cryst. Growth Des. 20 (2020) 6585–6591, https://doi.org/10.1021/acs.cgd.0c00756.
[45] M. Yang, Y. Qian, D. Yan, Y. Li, Y. Song, Z. Wang, C. Yi, H.L. Feng, H. Weng, Y. Shi, Magnetic and electronic properties of a topological nodal line semimetal candidate: HoSbTe, Phys. Rev. Mater. 4 (2020), 094203, https://doi.org/10.1103/PhysRevMaterials.4.094203.
[46] S. Yue, Y. Qian, M. Yang, D. Geng, C. Yi, S. Kumar, K. Shimada, P. Cheng, L. Chen, Z. Wang, H. Weng, Y. Shi, K. Wu, B. Feng, Topological electronic structure in the antiferromagnet HoSbTe, Phys. Rev. B. 102 (2020), 155109, https://doi.org/10.1103/PhysRevB.102.155109.
[47] F. Gao, J. Huang, W. Ren, M. Li, H. Wang, T. Yang, B. Li, Z. Zhang, Magnetic and transport properties of the topological compound DySbTe, Phys. Rev. B. 105 (2022), 214434, https://doi.org/10.1103/PhysRevB.105.214434.
[48] B. Bradlyn, L. Elcoro, J. Cano, M.G. Vergniory, Z. Wang, C. Felser, M.I. Aroyo, B. A. Bernevig, Topological quantum chemistry, Nature 547 (2017) 298–305, https://doi.org/10.1038/nature23268.
[49] J. Hu, Y. Zhu, X. Gui, D. Graf, Z. Tang, W. Xie, Z. Mao, Quantum oscillation evidence for a topological semimetal phase in ZrSnTe, Phys. Rev. B. 97 (2018), 155101, https://doi.org/10.1103/PhysRevB.97.155101.
[50] B. Chen, B. Zhang, J. Yu, F. Fei, M. Naveed, Y. Zhang, Z. Sun, X. Wan, F. Song, Observations of nodal lines in the topological semimetal ZrSnTe, Sci. China Phys., Mech. Astron. 63 (2019), 227011, https://doi.org/10.1007/s11433-019-9448-8.
[51] P.C. Canfield, Z. Fisk, Growth of single crystals from metallic fluxes, Philos. Mag. B 65 (1992) 1117–1123, https://doi.org/10.1080/13642819208215073.
[52] M.G. Kanatzidis, R. Pöttgen, W. Jeitschko, The metal flux: a preparative tool for the exploration of intermetallic compounds, Angew. Chem. Int. Ed. 44 (2005) 6996–7023, https://doi.org/10.1002/anie.200462170.
[53] ASM International, ASM Alloy Phase Diagram Database™. (n.d.). https://www.asminternational.org/materials-resources/online-databases/-/journal_content/56/10192/15469013/DATABASE/.
[54] J. Wang, P. Yox, K. Kovnir, Flux growth of phosphide and arsenide crystals, Front. Chem. 8 (2020). ⟨https://www.frontiersin.org/articles/10.3389/fchem.2020.00186⟩.
[55] B. Ji, K. Pandey, C.P. Harmer, F. Wang, K. Wu, J. Hu, J. Wang, Centrosymmetric or noncentrosymmetric? Transition metals talking in K2TGe3S8 (T= Co, Fe), Inorg. Chem. 60 (2021) 10603–10613.
[56] W. Zhou, H. Gao, J. Zhang, R. Fang, H. Song, T. Hu, A. Stroppa, L. Li, X. Wang, S. Ruan, W. Ren, Lattice dynamics of Dirac node-line semimetal ZrSiS, Phys. Rev. B. 96 (2017), 064103, https://doi.org/10.1103/PhysRevB.96.064103.
[57] E. Dong, R. Liu, S. Niu, X. Luo, K. Hu, H. Tian, B. Liu, X. Li, Y. Li, X. Zhu, Q. Li, B. Liu, Pressure-induced electronic and structural transition in nodal-line semimetal ZrSiSe, Inorg. Chem. 60 (2021) 11140–11146, https://doi.org/10.1021/acs.inorgchem.1c01087.
[58] H. Yuan, X. Zhou, Y. Cao, Q. Bian, Z. Zhang, H. Sun, S. Li, Z. Shao, J. Hu, Y. Zhu, Z. Mao, W. Ji, M. Pan, Raman detection of hidden phonons assisted by atomic point defects in a two-dimensional semimetal, npj 2D Mater. Appl. 3 (2019) 12, https://doi.org/10.1038/s41699-019-0093-7.
[59] H. Pan, B. Tong, J. Yu, J. Wang, D. Fu, S. Zhang, B. Wu, X. Wan, C. Zhang, X. Wang, F. Song, Three-dimensional anisotropic magnetoresistance in the dirac node-line material ZrSiSe, Sci. Rep. 8 (2018) 9340, https://doi.org/10.1038/s41598-018-27148-z.
[60] X. Wang, X. Pan, M. Gao, J. Yu, J. Jiang, J. Zhang, H. Zuo, M. Zhang, Z. Wei, W. Niu, Z. Xia, X. Wan, Y. Chen, F. Song, Y. Xu, B. Wang, G. Wang, R. Zhang, Evidence of both surface and bulk dirac bands and anisotropic nonsaturating magnetoresistance in ZrSiS, Adv. Electron. Mater. 2 (2016) 1600228, https://doi.org/10.1002/aelm.201600228.
[61] R. Singha, A.K. Pariari, B. Satpati, P. Mandal, Large nonsaturating magnetoresistance and signature of nondegenerate Dirac nodes in ZrSiS, Proc. Natl. Acad. Sci. 114 (2017) 2468–2473, https://doi.org/10.1073/pnas.1618004114.